



Article

Bifunctional Single-Atom Cobalt Electrocatalysts with Dense Active Sites Prepared via a Silica Xerogel Strategy for Rechargeable Zinc–Air Batteries

Lijuan Wang ¹, Zixiang Xu ¹, Tingyu Peng ², Maosong Liu ^{1,*}, Long Zhang ^{1,*} and Jianming Zhang ^{1,*}

¹ Institute of Quantum and Sustainable Technology (IQST), School of Chemistry and Chemical Engineering, Jiangsu University, Zhenjiang 212013, China; 2211912020@stmail.ujs.edu.cn (L.W.); 3191303039@stmail.ujs.edu.cn (Z.X.)

² Instrumental Analysis Center, Jiangsu University, Zhenjiang 212013, China; 1000005654@ujs.edu.cn

* Correspondence: 2112012005@stmail.ujs.edu.cn (M.L.); longzhang@ujs.edu.cn (L.Z.); zhangjm@ujs.edu.cn (J.Z.)

Abstract: The N-doped cobalt-based (Co) bifunctional single atom catalyst (SAC) has emerged as one of the most promising candidates to substitute noble metal-based catalysts for highly efficient bifunctionality. Herein, a facile silica xerogel strategy is elaborately designed to synthesize uniformly dispersed and dense Co-N_x active sites on N-doped highly porous carbon networks (Co-N-C SAC) using economic biomass materials. This strategy promotes the generation of massive mesopores and micropores for substantially improving the formation of Co-N_x moieties and unique network architecture. The Co-N-C SAC electrocatalysts exhibit an excellent bifunctional activity with a potential gap (ΔE) of 0.81 V in alkaline medias, outperforming those of the most highly active bifunctional electrocatalysts. On top of that, Co-N-C SAC also possesses outstanding performance in ZABs with superior power density/specific capacity. This proposed synthetic method will provide a new inspiration for fabricating various high-content SACs for varied applications.

Keywords: single-atom catalysts; ORR/OER; electrocatalysis; zinc–air battery; xerogel



Citation: Wang, L.; Xu, Z.; Peng, T.; Liu, M.; Zhang, L.; Zhang, J. Bifunctional Single-Atom Cobalt Electrocatalysts with Dense Active Sites Prepared via a Silica Xerogel Strategy for Rechargeable Zinc–Air Batteries. *Nanomaterials* **2022**, *12*, 381. <https://doi.org/10.3390/nano12030381>

Academic Editor: Christian M. Julien

Received: 16 December 2021

Accepted: 20 January 2022

Published: 24 January 2022

Publisher's Note: MDPI stays neutral with regard to jurisdictional claims in published maps and institutional affiliations.



Copyright: © 2022 by the authors. Licensee MDPI, Basel, Switzerland. This article is an open access article distributed under the terms and conditions of the Creative Commons Attribution (CC BY) license (<https://creativecommons.org/licenses/by/4.0/>).

1. Introduction

The metal–air battery has attracted considerable attention as a promising energy storage system due to its high theoretical energy/power density, reliable safety, and economic viability [1–4]. Among them, alkaline Zn–air batteries (ZABs) have been widely studied owing to the advantages of being cost-effective and their high theoretical energy density up to 1084 W h kg^{−1} [5–7]. However, the main impediment of their commercial application is the sluggish kinetics and poor durability of the oxygen evolution reaction (OER) and oxygen reduction reaction (ORR) on the air electrode [8–12]. Generally, the two reactions still need noble metal catalysts (such as Ir/Ru for OER, Pt for ORR), which suffer from the severely unavoidable deficiencies such as high cost, scarcity, and poor long-term stability [13–15]. Thus, marvelous efforts have been devoted to exploring cost-effective materials as the ORR and OER bifunctional catalyst with high activity to substitute precious Ru-, Ir-, and Pt-based catalyst, such as metal oxides, sulfides, hydroxides, single atom catalysts (SACs), and other hybrids [16–22]. Among all the previously reported non-precious metal catalysts, heteroatom-doped bifunctional SACs are attracting ever-growing interest for ZABs. For example, single atomic cobalt coordinated nitrogen (Co-N_x) moieties in the carbon matrix have been selected as promising low-cost substitutes for ZABs, contributing their elemental abundance, high atom utilization, and impressive bifunctional activity [5–7,23,24].

A series of strategies based on co-precipitation, wet impregnation, and metal–organic frameworks (MOFs) [25–27] have been recently developed for preparing Co-N-C SACs. Furthermore, many advanced biomass-derived electrocatalysts, e.g., nutshell and red bean

pod, have shown excellent electrocatalytic performance for metal–air batteries [28–30]. Despite significant progresses, there are still quite a few challenges to synthesize the well-defined metal–nitrogen co-doped carbon catalysts, including the aggregation of metal atoms at high temperature, harsh reaction conditions, and environmental pollutions. These side effects greatly limit exact investigations of the catalytic mechanism and activity [31,32]. In order to produce a high content of Co-N_x moieties in Co-N-C SACs for efficient OERs and ORRs, the pyrolysis of concentrated Co- and N-containing precursors with C source is the most prevailing manipulation for generating adequate active sites; however, the Co atoms inevitably tend to agglomerate and cluster into Co-based crystals or nanoparticles encapsulated by C, driven by their high surface free energy during thermal treatment. This phenomenon will be further intensified with the concentration increase in Co precursor, thereby seriously suppressing the formation of active Co-N_x sites as well as inducing decreased Co-loading in SACs (<1 wt%) [6,33–41]. Apart from the stabilization of Co, the porosity of the carbon matrix is another key factor for the OER and ORR activity, which exerts an important impact on hosting active sites and the accessibility of reactants to the three-phase boundary. In particular, micropores mainly host the Co-N_x active sites, and mesopores can facilitate the mass transport of reactants [42–44]. Thus, it is necessary to select a suitable substrate to assist the synthesis of densely well-defined SACs with optimized pore distribution.

Herein, we report a silica xerogel-assisted synthetic approach to fabricate atomically dispersed Co on a N-doped porous network C (shortened as Co-N-C SAC thereafter) using the Stöber method and naturally abundant materials of cobalt gluconate and glucosamine as the Co, N, and C precursors. Benefiting from the dense Co-N_x moieties and rational porous microstructure of the resultant C materials, the as-prepared Co-N-C SAC demonstrates excellent bifunctional OER/ORR activity with an overpotential ΔE of 0.81 V in alkaline medium, which is better than most of the bifunctional oxygen catalysts reported previously [45,46]. The assembled ZAB using the Co-N-C SACs shows a high open-circuit voltage of 1.49 V, a high-power density of 143.1 mW cm⁻², and high specific capacity (942 mA h g⁻¹) at 10 mA cm⁻², surpassing the commercial 20% Pt/C + IrO₂ catalyst and most of the non-precious-metal catalysts [47–49]. This facile strategy, based on biomass-derived precursors, can open an avenue for the large-scale commercial production of single-atom catalysts.

2. Experimental Section

2.1. Materials

Sodium gluconate, glucosamine hydrochloride, cobalt chloride hexahydrate (CoCl₂·6H₂O), tetraethyl orthosilicate (TEOS), ammonia (25–28 wt%), and absolute ethanol were all analytical grade, commercially available from Shanghai Chemical Reagent Co., Ltd. (Shanghai, China), and used without further purification. The commercial Pt/C (20 wt%) and IrO₂ catalysts were purchased from Johnson Matthey Corporation (London, UK). Deionized water (18 MΩ·cm) was used in the whole experiments.

2.2. Synthesis of Co-N-C SAC Catalyst

Glucosamine hydrochloride (1.5 g), sodium gluconate (0.3 g), and CoCl₂·6H₂O (0.15 g) were first dissolved in 13 mL of H₂O containing 50 μL of ammonia. Then, absolute ethanol (10 mL) and TEOS (10 mL) were introduced to the above transparent mixture and kept for 3 h at 60 °C under stirring to form the glucose/SiO₂ sol–gel. Glucose/SiO₂ xerogels were obtained by freeze drying the resulting sol–gel for 12 h. The dry powder was subsequently ground with the same quantity of urea, which was followed by transferring the crude into a furnace and pyrolyzing at 900 °C for 2 h under the argon (Ar) atmosphere. The pyrolyzed sample (denoted as Co-N-C/SiO₂) was etched using a hydrofluoric acid solution to remove silica and Co particles. The acid-washed sample was thermal-treated at 900 °C for another 2 h in Ar to form the final product of Co-N-C SAC. Using the same protocol

as the preparation of Co-N-C SAC, the N-C control catalyst was prepared in the absence of $\text{CoCl}_2 \cdot 6\text{H}_2\text{O}$.

3. Characterizations

Transmission electron microscopy (TEM) and X-ray photoelectron spectroscopic (XPS) measurements were performed using Talos-200X with EDS analysis and ESCALAB Xi+, respectively (Thermo Fisher Scientific, Waltham, MA, USA). Scanning electron microscopy (SEM) was tested using a JSM-7800 (JEOL Co., Ltd., Tokyo, Japan). XPS peak energies were calibrated by placing the graphite C 1s peak at 284.6 eV. The aberration-corrected high-angle annular dark-field scanning TEM (HAADF-STEM) was conducted using a Spectra 300 at the Center for Electron Microscopy of Thermo Fisher Scientific, Eindhoven, Netherlands. X-ray diffraction (XRD) was investigated using a Rotaflex D/MAX-2500 (Rigaku Co., Ltd., Tokyo, Japan), with Cu $K\alpha$ radiation ($\lambda = 1.54178 \text{ \AA}$). BET experiments were conducted at 77 K on a Quantachrome AUTOSORB IQ Instrument (Anton Paar Quanta Tec Inc., Boynton Beach, FL, USA). The surface areas were estimated from the Brunauer–Emmett–Teller (BET) equation by fitting the N_2 -adsorption isotherms from 0.05 to 0.3 (P/P_0 range). Raman spectra were recorded using a Thermo Fisher DXR (Thermo Fisher Scientific) with an incident laser wavelength of 532 nm.

3.1. Electrochemical Measurements

The electrochemical measurements were conducted using a CHI 760D potentiostat with a one-component three-electrode cell in 0.1 M KOH electrolyte. A platinum wire and an Ag/AgCl electrode were used as the counter and reference electrode, respectively. The working electrode was a glassy-carbon (GC) rotating ring disk electrode (RRDE) (diameter: 5 mm, area: 0.196 cm^2) purchased from Pine Instruments (Grove City, PA, USA). The measured potential against Ag/AgCl was converted to an RHE value using the Nernst equation: $E_{\text{RHE}} = E_{\text{Ag/AgCl}} + 0.059 \text{ pH} + 0.197$. All the measurements were measured at ambient conditions. The catalyst ink was prepared by dispersing 5 mg of the catalyst into 480 μL ethanol containing 40 μL of Nafion (5%). Then, the catalyst ink was deposited on the GC electrode with an overall catalyst loading of 0.3 mg cm^{-2} . The cyclic voltammetry (CV) curves were recorded in both N_2 - and O_2 -saturated electrolytes with a 50 mV s^{-1} of scan rate. In contrast, commercial 20 wt% Pt/C and IrO_2 catalyst (Johnson Matthey, JM) was used as the control catalyst, and the Pt loading was 0.1 mg cm^{-2} . The ORR and OER activity were determined by linear scanning voltammetry (LSV) on an RRDE in an O_2 -saturated and N_2 -saturated 0.1 M KOH solution with a rotating speed of 1600 rpm, respectively. All LSV measurements of the catalysts were measured using an RRDE.

The Koutecky–Levich (K – L) plots can be obtained by linear fitting of the reciprocal rotating speed versus reciprocal current density collected at -0.2 V , -0.3 V , -0.4 V , -0.5 V , and -0.6 V , respectively. The electron transfer number (n) of the sample can be calculated by K – L plots according to the ORR-LSV data at different rotation rates (Equations (1) and (2)).

$$\frac{1}{J} = \frac{1}{J_K} + \frac{1}{J_L} = \frac{1}{J_K} + \frac{1}{B} \omega^{-\frac{1}{2}} \quad (1)$$

$$B = 0.2nF \left(D_{(\text{O}_2)} \right)^{\frac{2}{3}} \nu^{-\frac{1}{6}} C_{(\text{O}_2)} \quad (2)$$

where J and J_K are the measured current density and kinetic current density, respectively, F is the Faraday constant (96485 C mol^{-1}), $D_{(\text{O}_2)}$ is the diffusion coefficient of O_2 in 0.1 M KOH ($1.9 \times 10^{-5} \text{ cm}^2 \text{ s}^{-1}$), ν is the kinetic viscosity coefficient of electrolyte ($0.01 \text{ cm}^2 \text{ s}^{-1}$), $C_{(\text{O}_2)}$ is the bulk concentration of O_2 in the electrolyte ($1.2 \times 10^{-6} \text{ mol cm}^{-3}$), and ω is the electrode rotation speed (rpm).

The electron transfer number (n) and hydrogen peroxide yield (% H_2O_2) during the ORR can be determined by the RRDE technique:

$$\text{H}_2\text{O}_2(\%) = 200 \times \frac{\frac{I_r}{N}}{I_d + \frac{I_r}{N}}$$

$$n = 4 \times \frac{I_d}{I_d + \frac{I_r}{N}}$$

where I_d is the disk current, I_r is the ring current, and $N = 0.37$ is the current collection efficiency of the Pt ring.

3.2. Zn–Air Battery

The Zn–air battery was tested in a home-made electrochemical cell. The catalysts were loaded on a gas diffusion layer/carbon paper (2 mg cm^{-2}). A Pt/C electrode with the same catalyst loading was also prepared as a comparative control. The commercial Zn foil was used as cathode and 6 M KOH was used as electrolyte containing 0.2 M $\text{Zn}(\text{Ac})_2$. All the measurements were performed on the as-constructed cell at room temperature with CHI 760D electrochemical workstation (CH Instruments, Shanghai, China).

The specific capacity is calculated using the data obtained from the measured constant current discharge curves.

$$\text{specific capacity} = \frac{\text{current density} \times \text{test hours}}{\text{consumed zinc plate mass}}$$

4. Results and Discussion

4.1. Synthesis Protocol

Figure 1 shows the schematic illustration of the overall synthetic process of Co-N-C SACs, which mainly includes three key steps. (i) First, there is the synthesis of the precursor in SiO_2 so–gel. A classic Stöber approach was used to prepare the sol–gel, in which cobalt gluconate and glucosamine were mixed with TEOS (SiO_2 precursor) for hydrolysis. This important step produces the SiO_2 sol–gel with a uniform filling of Co, N, and C precursor solution in the 3D networks. (ii) Next, there is freeze drying, pyrolysis, and acid etching. Here, the volatiles (i.e., water, ethanol, and ammonia) adsorbed in the sol–gel system were readily evaporated upon freeze drying, leading to the formation of a SiO_2 xerogel with cobalt gluconate and glucosamine molecules distributing homogeneously within the 3D frameworks of SiO_2 . Then, the xerogel system was pyrolyzed under an inert atmosphere to transfer the precursors into N-doped C and Co species supported by the SiO_2 frames. In order to remove the SiO_2 and undesirable substances, the annealed product was etched using hydrofluoric acid and treated by a post-thermal approach, eventually leading to the production of isolated single Co atoms anchored porous N-doped C materials. In contrast, a control N-C sample was synthesized using the same procedures without cobalt gluconate.

The 3D network of SiO_2 xerogel acts as a hard template and protector during preparation, which can efficiently trap precursor molecules, stabilize the free migration of Co species, and prevent the congestion of Co nanoparticles/clusters [33,37,50,51]. The porosity and surface area of the resultant N-doped porous C networks can be greatly increased while removing the SiO_2 xerogel and hence promote the exposure of active sites and mass transfer. Interestingly, the Co content can be facily tuned-up to 2.38 wt% (confirmed by XPS). With this method, one is able to synthesize the Co-N-C SAC with a high amount of 100 g/batch at the laboratory scale.

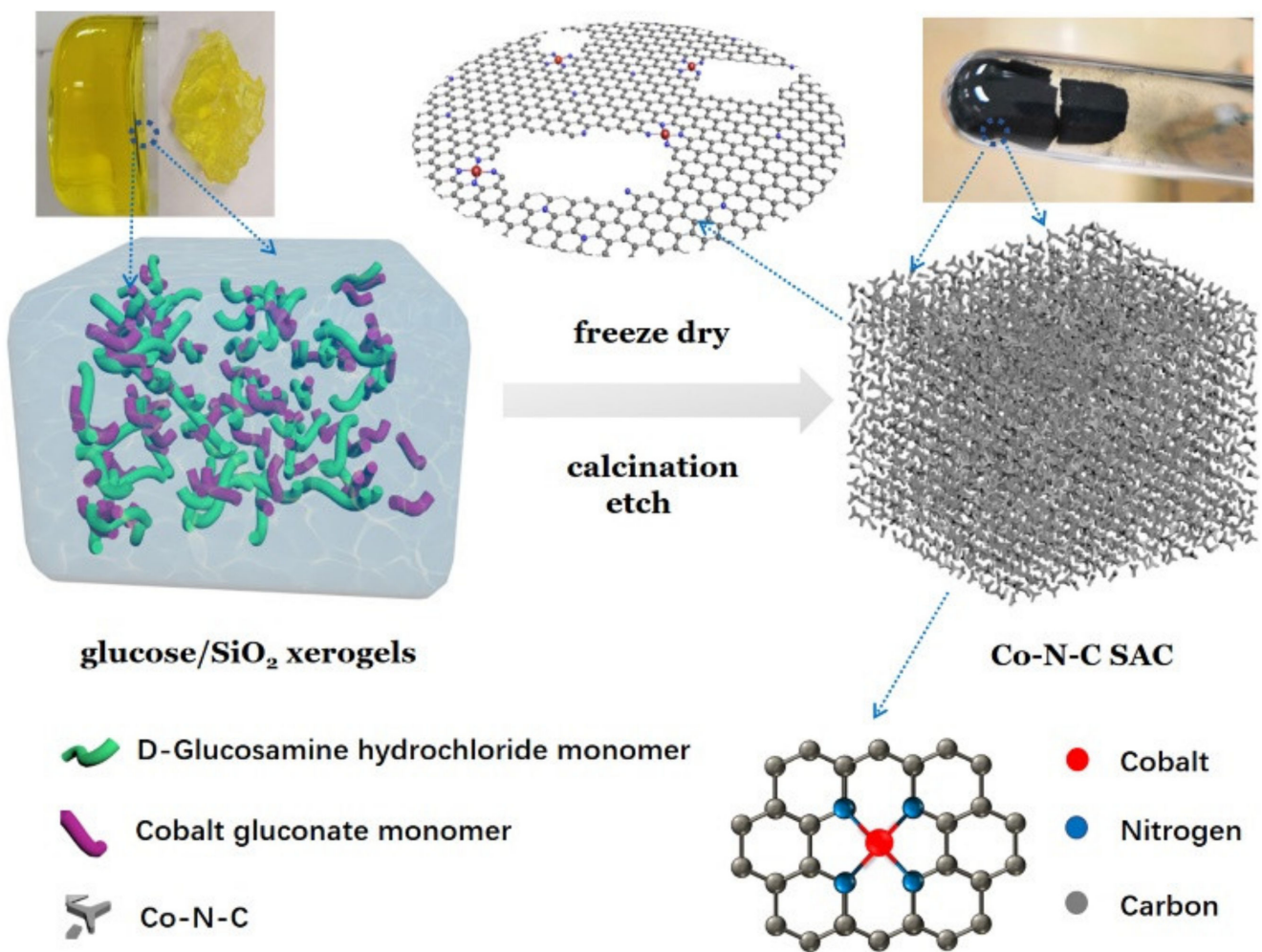


Figure 1. Schematic representation of the synthesis of Co-N-C SACs.

4.2. Morphological Features

The surface morphologies of Co-N-C SAC are presented in Figures 2a–e and S1 via TEM and SEM. Co-N-C SAC shows the porous and disordered morphology (Figure 2a–c), and there are no obvious aggregates or nanoparticles. TEM and SEM images of the N-C sample also show the similar structure feature (Figure S2a,b). The high-resolution TEM image in Figure 2c reveals that the sample is constituted of distorted multilayer structures with an interplanar distance of ca. 0.34 nm, which is in good agreement with the typical features of graphite-like carbon (i.e., lattice spacing of {101} facet for graphite). To verify the formation of Co single atoms in the Co-N-C SAC, HAADF-STEM measurements were further performed. As exhibited in Figure 2d, plenty of bright spots with the size of around 0.2 nm are well distributed along the carbon support, corresponding to the individually dispersed Co atoms. This observation strongly confirms the presence of single atomic Co in the sample. Energy-dispersive spectrometer (EDS) mapping (Figure 2e) analysis was carried out, suggesting the Co, N, and C are distributed uniformly in the carbon matrix. Therefore, the TEM characterization of the Co-N-C SAC strongly indicates that our xerogel synthetic approach can be successfully applied to disperse Co single-atom species in the three-dimensional (3D) porous carbon networks.

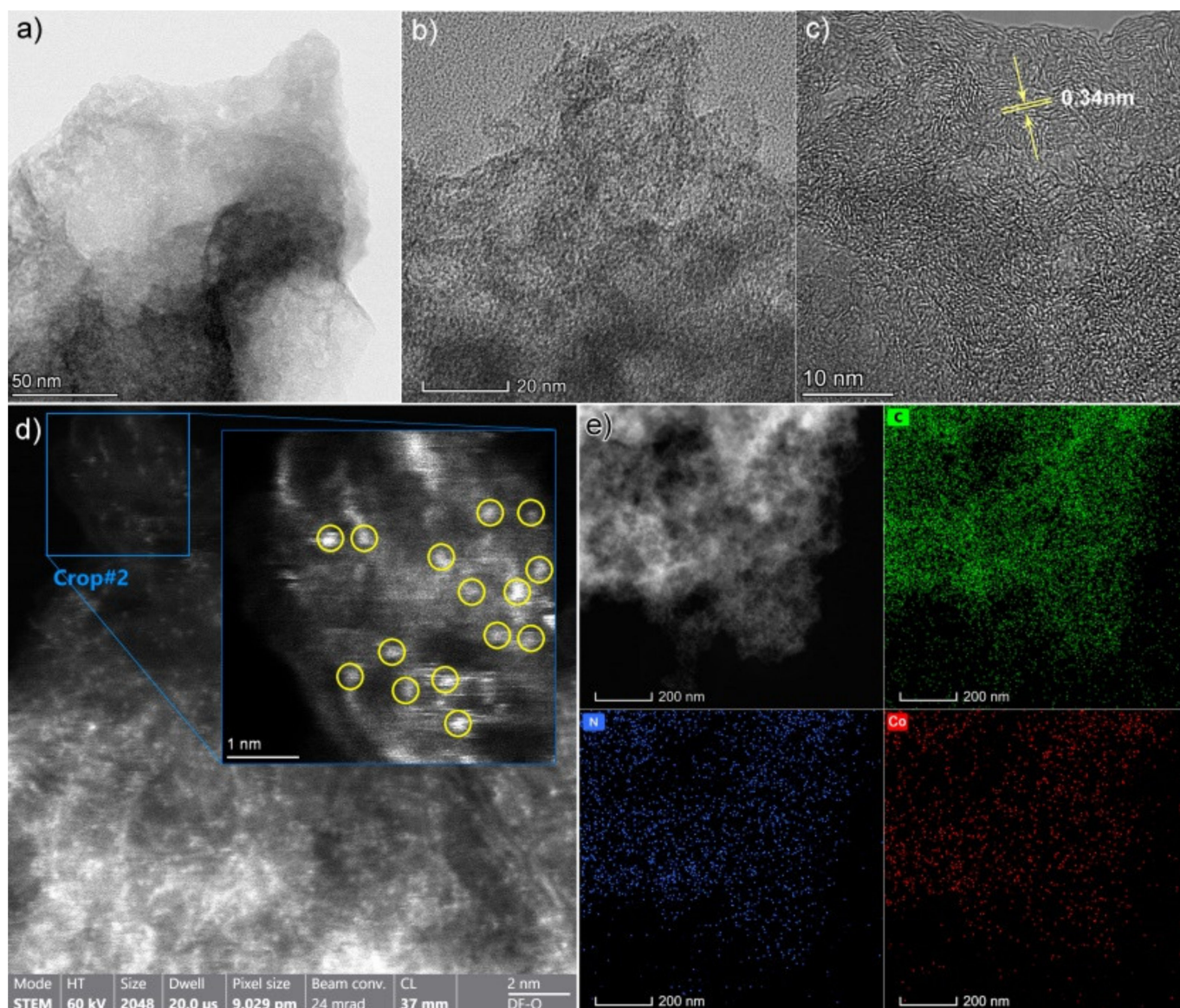


Figure 2. (a,b) TEM, (c) HRTEM, and (d) HAADF-STEM images of the Co-N-C SAC. Bright spots in (d) indicate the single Co metal atoms marked with a yellow circle dispersed in the carbon matrix. (e) Dark-field TEM image of the selected area for EDS elemental mapping images of C, N, and Co in the Co-N-C SAC.

4.3. Structural Features

The samples were also examined using XRD spectroscopy. The XRD pattern (Figure 3a) of Co-N-C SAC and N-C shows wide peaks at $\approx 25.7^\circ$ and $\approx 44.0^\circ$, which may be attributed to the diffractions of {002} and {101} planes of graphitic carbon, respectively. Obviously, there is no distinct diffraction peak induced by metallic Co or other Co-based crystals, hence confirming the formation of atomically dispersed Co single atoms in the samples. Complementary to TEM observations, the Raman spectra of the Co-N-C SAC and N-C offered the structural defect and chemical composition (Figure 3b), which closely link to their electrocatalytic performance of the ORR and OER. Figure 3b shows the deconvoluted spectra of the Co-N-C SAC and N-C sample, indicating a G band and D band at peaks of $\approx 1590 \text{ cm}^{-1}$ and at $\approx 1350 \text{ cm}^{-1}$, respectively. The calculated intensity ratios of I_D/I_G for Co-N-C SAC and N-C are 1.08 and 0.98, respectively, which confirms the presence of amorphous carbon of Co-N-C SAC with a lower graphitization degree than the N-C one.

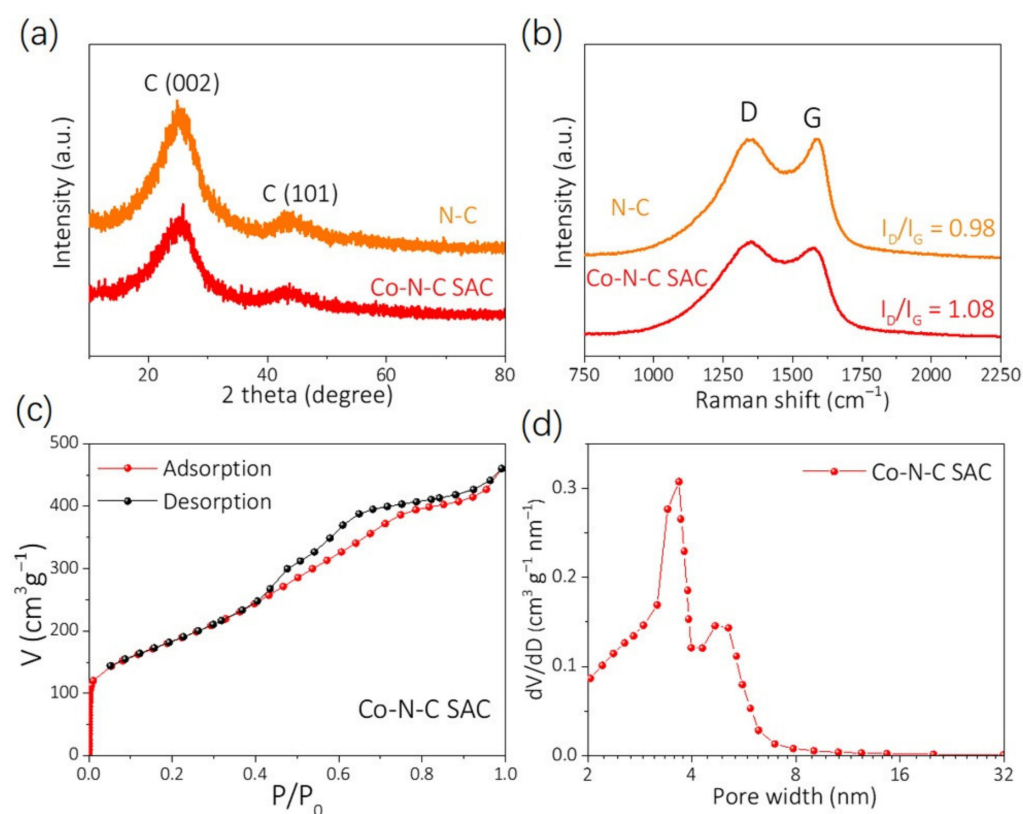


Figure 3. (a) XRD pattern and (b) Raman spectra of Co-N-C SAC and N-C. (c) Nitrogen adsorption/desorption isotherm and (d) BJH pore size distribution plot of Co-N-C SAC.

The porosity of the carbon support critically influences the mass transport between the catalyst surface and the bulk solution [42,43]. The N_2 adsorption/desorption isotherm and type-IV adsorption isotherm for Co-N-C SAC are illustrated in Figure 3c. The Co-N-C SAC presented a steep increase in V_{ads} at a relatively low N_2 pressure ($P/P_0 = 0-0.015$) and a well-defined hysteresis loop at a higher N_2 pressure ($P/P_0 = 0.4-0.9$), indicating the coexistence of micro and mesopores [43,52]. The surface area of Co-N-C SAC is $737 \text{ m}^2 \text{ g}^{-1}$ calculated from the isotherm via BET, and the Barret, Joyner, and Halenda (BJH) pore size distribution indicates that the pore diameters are in the range of 3–6 nm (Figure 3d). Figure S3 displays the cumulative pore volume. Obviously, Co-N-C SAC mainly contains micropores and mesopores with 2–10 nm size range, and the Co-N-C SAC shows a sharp increase in pore volume when the mesopores are less than 10 nm. The BET surface area analysis and TEM characterizations (Figure 2) suggest that the Co-N-C SAC consists of a homogeneous disordered 3D porous network architecture with a large amount of micropores and mesopores, in which the micropores host most of the active sites to drive the reaction [53,54], and mesopores mainly provide the channels for reactant exchange [43]. Therefore, the Co-N-C SAC is expected to show excellent catalytic performance in ZABs.

XPS measurements were carried out for studying the surface composition and chemical state of Co-N-C SAC. The XPS survey spectra of Co-N-C SAC show C 1s, N 1s, and Co 2p signals in the sample (Figure 4a). The high-resolution spectra of C 1s, N 1s, and Co 2p were also recorded for obtaining deep insight into the individual elements in Co-N-C SAC. As shown in Figure 4b–d, the Co 2p spectrum after deconvolution presents two pairs of peaks for Co^{2+} (795.6 and 780.1 eV) and Co^{3+} (802.1 and 782.7 eV) with a satellite peak at ≈ 786.3 eV, and no signal of metallic Co (Co^0) is detected. The N 1s spectrum in Figure 4c can be deconvoluted into four distinct peaks, including the species of pyridinic-N (≈ 397.9 eV), pyrrolic-N (≈ 399.8 eV), graphitic-N (≈ 400.6 eV), and oxidized-N (≈ 403.3 eV). The N content in Co-N-C SAC was determined to be as high as 10.74 wt% (Table S1). It has been reported that the pyridinic-N plays a crucial role to generate $Co-N_x$ active sites, while

graphitic N affects the geometry and electronic structure of the carbon matrix [50,55,56]. The C 1s spectrum displays four peaks at 290.4, 287.5, 285.6, and 284.2 eV, which can be assigned to the C=O, C-O, C-N, and C-C group, respectively (Figure 4d).

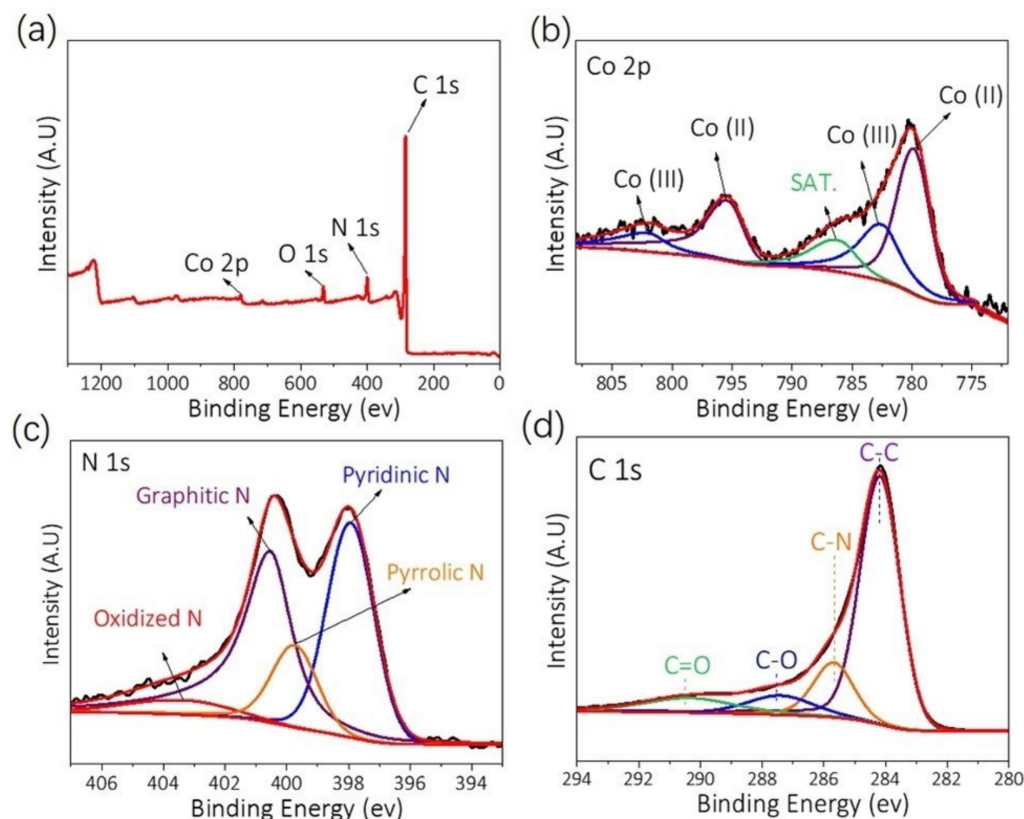


Figure 4. (a) XPS survey spectrum of Co-N-C SAC. Deconvoluted XPS spectra of (b) Co 2p, (c) N 1s, and (d) C 1s for Co-N-C SAC.

4.4. Electrochemical Measurements

The liner sweep voltammograms (LSVs) and cycle voltammograms (CVs) of the synthesized samples were used to evaluate the ORR performance in N_2 - and O_2 -saturated KOH electrolyte. The Co-N-C SAC exhibits greatly improved performance of onset potential ($E_{onset} = 1.01$ V vs. RHE), as shown in Figure 5a, which are more active than a commercial 20% Pt/C ($E_{onset} = 0.97$ V vs. RHE), N-C ($E_{onset} = 0.90$ V vs. RHE) and the reference catalysts reported recently (Table S2). The Co-N-C SAC demonstrates the good ORR performance with the highest half-wave potential ($E_{1/2}$) value of 0.851 V and an obviously enlarged diffusion-limited current density (J_{lim}) about 5.92 mA cm^{-2} at 0.2 V vs. RHE (Figure 5a). The performance is similar to the 20% Pt/C catalyst ($E_{1/2}$ 0.847 V, J_{lim} 5.89 mA cm^{-2}) and better than N-C catalyst ($E_{1/2}$ 0.794 V, J_{lim} 4.15 mA cm^{-2}). Figure 5b shows the Tafel slopes of these samples, where Co-N-C SAC represents an attractive Tafel slope of 78.3 mV dec^{-1} , which is smaller than that of Pt/C (86.5 mV dec^{-1}) and N-C (89.7 mV dec^{-1}), indicating that Co-N-C SAC shows more favorable ORR kinetics ascribed to the acceleration of mass and electron transport in 3D interconnected mesopores carbon networks of Co-N-C SAC [53,54]. Furthermore, the calculated electron transfer number (n) (Figure S4) was obtained according to Koutecky–Levich ($K-L$) plots for studying the ORR kinetics of Co-N-C SAC. The n is calculated to be close to 4, indicating that the catalyst undergoes a catalytic process via a four-electron pathway with high-efficiency. Figure S5 shows that the H_2O_2 yield is lower than 10% detected on the Pt ring.

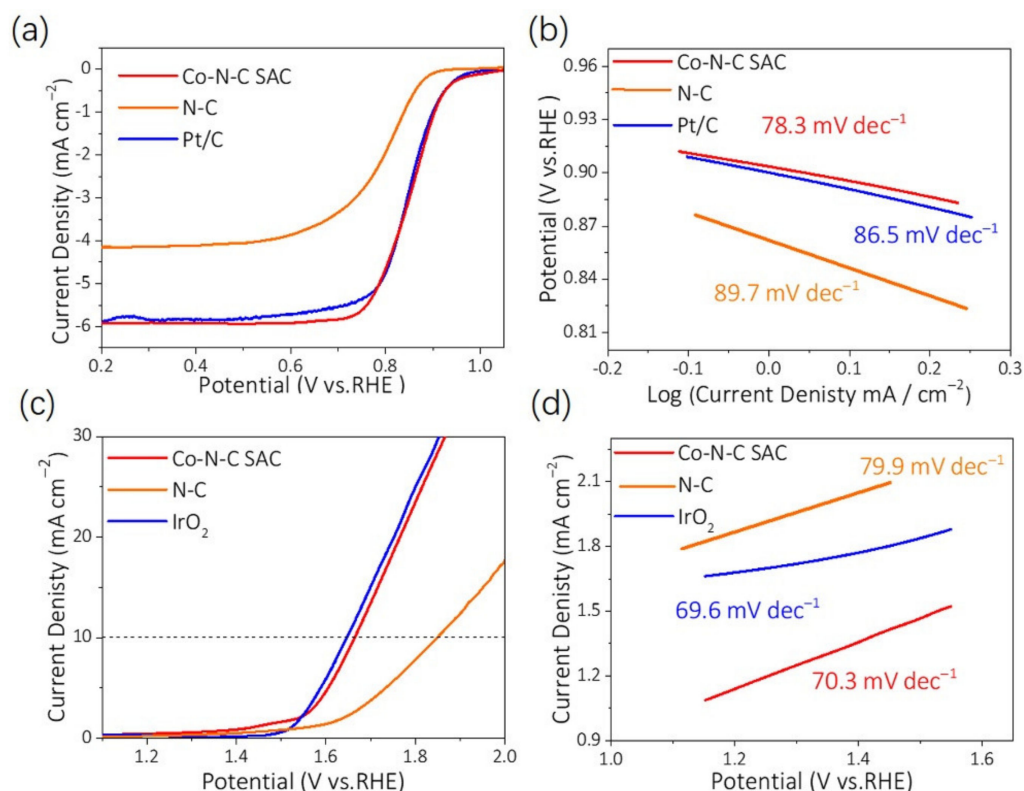


Figure 5. (a) ORR polarization curves and (b) corresponding Tafel plots of Co-N-C SAC. (c) OER polarization curves and (d) corresponding Tafel plots of Co-N-C SAC.

To evaluate the bifunctionality of the catalysts for rechargeable ZAB, the OER performances of the catalysts were also measured in a 0.1 M KOH electrolyte. As illustrated by the LSV results in Figure 5c,d, the overpotentials required to reach the current density of 10 mA cm^{-2} is 430 mV, 618 mV, and 400 mV for Co-N-C SAC, N-C, and IrO_2 , respectively. The overpotential of Co-N-C SAC is lower than the N-C sample and comparable to that of IrO_2 . Additionally, Co-N-C SAC demonstrates a lower Tafel slope of 70.3 mV dec^{-1} , which is significantly smaller than those of N-C (79.9 mV dec^{-1}), suggesting a faster OER catalytic kinetics (Figure 5d) perhaps on the basis of the higher amount of atomically dispersed Co species and larger surface area.

4.5. Zn–Air Battery Performance

Beyond traditional electrochemical investigations in standard three-electrode systems, the homemade primary and rechargeable ZABs were also fabricated to further examine the performance of Co-N-C SAC as air cathode catalyst. The ZAB was equipped with 6 M KOH containing 0.2 M $\text{Zn}(\text{Ac})_2$ as electrolyte, and a zinc plate and Co-N-C SAC-loaded carbon paper (1 mg/cm^2) was regarded as the anode and air cathode, respectively. In contrast, the 20% Pt/C + IrO_2 counterpart was also assembled. The open-circuit voltage of the Co-N-C SAC-based battery is 1.49 V, which is superior to the Pt/C + IrO_2 counterpart of 1.45 V (Figure 6a). Furthermore, two homemade ZABs light up an LED (1.5–5 V) panel lamp, demonstrating the successful operation of the ZAB (Figure 6a inset). The specific capacity of the ZAB using a cathodic Co-N-C SAC-based catalyst (Figure 6b) is calculated to be $779.8 \text{ mA h g}^{-1}$ at 10 mA cm^{-2} , which is slightly higher than the system using 20% Pt/C + IrO_2 with $738.3 \text{ mA h g}^{-1}$. The corresponding energy density of the Co-N-C SAC-based battery reaches 942 Wh kg^{-1} at 10 mA cm^{-2} , which is also superior to that of the Pt/C-based one (884 Wh kg^{-1}).

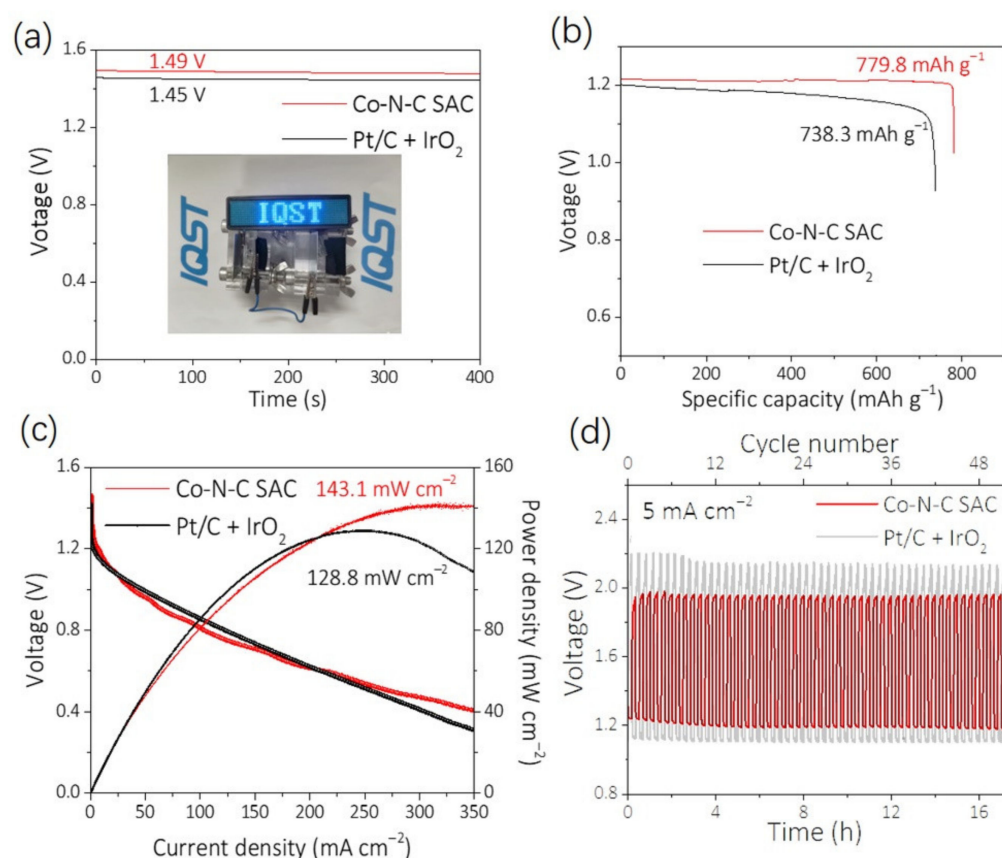


Figure 6. (a) Open-circuit plots of Co-N-C SAC and 20% Pt/C + IrO₂ (inset: Optical image of an LED light array powered by two ZABs in series using Co-N-C SAC as the air cathode). (b) Specific capacities of the ZABs using Co-N-C SAC and 20% Pt/C + IrO₂ as catalysts, which are normalized to the mass of the completely consumed Zn. (c) Polarization and power density curves for primary ZABs. (d) Charge–discharge cycling performance of Co-N-C SAC-based ZABs and 20% Pt/C+IrO₂-based ZABs with a duration of 20 min per cycle at 5 mA cm^{−2}.

The power density of battery is another vital parameter, reflecting the quality of the battery. Figure 6c presents the discharging polarization curves of the Co-N-C SAC and 20% Pt/C + IrO₂-based ZAB; the maximum power density of the Co-N-C SAC-based battery reaches 143.1 mW cm^{−2}, exceeding that of its 20% Pt/C + IrO₂-based counterpart (128.8 mW cm^{−2}) and most of the reported non-precious metal catalysts in this field [49]. The stability of the Co-N-C SAC-based battery was also assessed by a rechargeable ZAB, as shown in Figure 6d, where the initial discharging voltage is 1.18 V and charging voltage is 1.96 V for the Co-N-C SAC-based battery at the current density of 5 mA cm^{−2}. The charging–discharging voltage gap of the Co-N-C SAC-based battery maintains the initial overpotential of 0.78 V without any decay after a consecutive 54 cycles' scanning, indicating the long-term stability of the Co-N-C SAC-based ZAB. Obviously, the Co-N-C SAC-based battery delivers a lower charge–discharge voltage gap compared with the 20% Pt/C + IrO₂-based one (1.01 V), indicating a better rechargeability. All these outcomes suggest that the Co-N-C SAC can be employed as a promising electrode material for the potential application in the rechargeable ZABs.

5. Conclusions

In summary, we have presented a facile silica xerogel-assisted synthetic strategy to disperse Co single atoms on a N-doped porous network carbon as electrocatalyst for high-efficiency ORR/OER in alkaline medium. The synthesized Co-N-C SAC demonstrates excellent bifunctional performance due to the high-content Co-N_x active sites, massive

mesopores, and micropores of carbon matrix. The assembled Zn-air battery using the Co-N-C SAC exhibits outstanding specific energy of $779.8 \text{ mA h g}^{-1}$ at 10 mA cm^{-2} , excellent power density of 143.1 mW cm^{-2} , and moderately durability. This robust silica xerogel strategy is expected to fabricate various SACs with dense accessible active sites, high porosity, and surface area for broad application.

Supplementary Materials: The following supporting information can be downloaded at: <https://www.mdpi.com/article/10.3390/nano12030381/s1>, Figure S1: (a,b) SEM images of the Co-N-C SAC. Figure S2: (a) SEM and (b) TEM images of the N-C sample. Figure S3: Cumulative pore volume for Co-N-C SAC. Figure S4: (a) ORR LSV at different rates, (b) $K-L$ plots of Co-N-C SAC. Figure S5: The H_2O_2 yield and number of electron transfer at Co-N-C SAC and Pt/C. Table S1: Mass fraction content of C, N, O, and Co in Co-N-C SAC extracted from XPS measurements. Table S2: The onset potential of each catalyst in this work during ORR compared to the recent literature.

Author Contributions: Conceptualization, L.W. and M.L.; methodology, M.L.; validation, L.W., Z.X. and T.P.; formal analysis, L.W. and M.L.; data curation, Z.X. and T.P.; writing—original draft preparation, L.W., M.L.; writing—review and editing, L.Z., J.Z.; visualization, J.Z.; supervision, J.Z.; project administration, L.Z., J.Z.; funding acquisition, J.Z. All authors have read and agreed to the published version of the manuscript.

Funding: This research was funded by the National Natural Science Foundation of China (NSFC No. 51872128), Natural Science Foundation for Young Scholars of Jiangsu Province (Grant No. BK20210744), and the Young Talent Support Fund from Jiangsu University (Grant No. 4111310027).

Institutional Review Board Statement: Not applicable.

Informed Consent Statement: Not applicable.

Data Availability Statement: The data that support the findings of this study are available from the corresponding authors upon reasonable request.

Acknowledgments: We are grateful to the NanoPort of ThermoFisher Scientific at Shanghai and Europe (Eindhoven, Netherlands) for their help of the TEM observation and analysis to our samples.

Conflicts of Interest: The authors declare no conflict of interest.

References

1. Li, Y.; Gong, M.; Liang, Y.; Feng, J.; Kim, J.-E.; Wang, H.; Hong, G.; Zhang, B.; Dai, H. Advanced Zinc–Air Batteries Based on High-Performance Hybrid Electrocatalysts. *Nat. Commun.* **2013**, *4*, 1805. [[CrossRef](#)] [[PubMed](#)]
2. Meng, F.; Zhong, H.; Bao, D.; Yan, J.; Zhang, X. In Situ Coupling of Strung Co_4N and Intertwined N–C Fibers toward Free-Standing Bifunctional Cathode for Robust, Efficient, and Flexible Zn–Air Batteries. *J. Am. Chem. Soc.* **2016**, *138*, 10226–10231. [[CrossRef](#)] [[PubMed](#)]
3. Mistry, H.; Varela, A.S.; Kühn, S.; Strasser, P.; Cuenya, B.R. Nanostructured Electrocatalysts with Tunable Activity and Selectivity. *Nat. Rev. Mater.* **2016**, *1*, 16009. [[CrossRef](#)]
4. Ratso, S.; Walke, P.R.; Mikli, V.; Ločs, J.; Šmits, K.; Vītola, V.; Šutka, A.; Kruusenberg, I. CO_2 Turned into a Nitrogen Doped Carbon Catalyst for Fuel Cells and Metal–Air Battery Applications. *Green Chem.* **2021**, *23*, 4435–4445. [[CrossRef](#)]
5. Tang, C.; Wang, B.; Wang, H.-F.; Zhang, Q. Defect Engineering toward Atomic Co– N_x –C in Hierarchical Graphene for Rechargeable Flexible Solid Zn–Air Batteries. *Adv. Mater.* **2017**, *29*, 1703185. [[CrossRef](#)]
6. Yang, L.; Shi, L.; Wang, D.; Lv, Y.; Cao, D. Single-Atom Cobalt Electrocatalysts for Foldable Solid-State Zn–Air Battery. *Nano Energy* **2018**, *50*, 691–698. [[CrossRef](#)]
7. Xu, R.; Wang, X.; Zhang, C.; Zhang, Y.; Jiang, H.; Wang, H.; Su, G.; Huang, M.; Toghan, A. Engineering Solid–Liquid–Gas Interfaces of Single-Atom Cobalt Catalyst for Enhancing the Robust Stability of Neutral Zn–Air Batteries under High Current Density. *Chem. Eng. J.* **2021**, *431*, 133685. [[CrossRef](#)]
8. Jiang, W.-J.; Gu, L.; Li, L.; Zhang, Y.; Zhang, X.; Zhang, L.-J.; Wang, J.-Q.; Hu, J.-S.; Wei, Z.; Wan, L.-J. Understanding the High Activity of Fe–N–C Electrocatalysts in Oxygen Reduction: Fe/Fe₃C Nanoparticles Boost the Activity of Fe–N_x. *J. Am. Chem. Soc.* **2016**, *138*, 3570–3578. [[CrossRef](#)]
9. Lai, Q.; Zheng, L.; Liang, Y.; He, J.; Zhao, J.; Chen, J. Metal–Organic–Framework–Derived Fe–N/C Electrocatalyst with Five-Coordinated Fe–N_x Sites for Advanced Oxygen Reduction in Acid Media. *ACS Catal.* **2017**, *7*, 1655–1663. [[CrossRef](#)]
10. Li, J.-C.; Hou, P.-X.; Zhao, S.-Y.; Liu, C.; Tang, D.-M.; Cheng, M.; Zhang, F.; Cheng, H.-M. A 3D Bi-functional Porous N-doped Carbon Microtube Sponge Electrocatalyst for Oxygen Reduction and Oxygen Evolution Reactions. *Energy Environ. Sci.* **2016**, *9*, 3079–3084. [[CrossRef](#)]

11. Sumboja, A.; Lübke, M.; Wang, Y.; An, T.; Zong, Y.; Liu, Z. All-Solid-State, Foldable, and Rechargeable Zn-Air Batteries Based on Manganese Oxide Grown on Graphene-Coated Carbon Cloth Air Cathode. *Adv. Energy Mater.* **2017**, *7*, 1700927. [[CrossRef](#)]
12. Wang, H.-F.; Tang, C.; Wang, B.; Li, B.-Q.; Zhang, Q. Bifunctional Transition Metal Hydroxysulfides: Room-Temperature Sulfurization and Their Applications in Zn–Air Batteries. *Adv. Mater.* **2017**, *29*, 1702327. [[CrossRef](#)] [[PubMed](#)]
13. Nie, Y.; Li, L.; Wei, Z. Recent Advancements in Pt and Pt-free Catalysts for Oxygen Reduction Reaction. *Chem. Soc. Rev.* **2015**, *44*, 2168–2201. [[CrossRef](#)] [[PubMed](#)]
14. Li, Y.; Zhou, W.; Wang, H.; Xie, L.; Liang, Y.; Wei, F.; Idrobo, J.-C.; Pennycook, S.J.; Dai, H. An Oxygen Reduction Electrocatalyst Based on Carbon Nanotube–Graphene Complexes. *Nat. Nanotech.* **2012**, *7*, 394–400. [[CrossRef](#)]
15. Wang, J.; Liu, W.; Luo, G.; Li, Z.; Zhao, C.; Zhang, H.; Zhu, M.; Xu, Q.; Wang, X.; Zhao, C.; et al. Synergistic Effect of Well-Defined Dual Sites Boosting the Oxygen Reduction Reaction. *Energy Environ. Sci.* **2018**, *11*, 3375–3379. [[CrossRef](#)]
16. Li, B.-Q.; Zhang, S.-Y.; Tang, C.; Cui, X.; Zhang, Q. Anionic Regulated NiFe (Oxy)Sulfide Electrocatalysts for Water Oxidation. *Small* **2017**, *13*, 1700610. [[CrossRef](#)]
17. Lee, D.U.; Xu, P.; Cano, Z.P.; Kashkooli, A.G.; Park, M.G.; Chen, Z. Recent Progress and Perspectives on Bi-functional Oxygen Electrocatalysts for Advanced Rechargeable Metal–Air Batteries. *J. Mater. Chem. A* **2016**, *4*, 7107–7134. [[CrossRef](#)]
18. Cheng, F.; Chen, J. Metal–Air Batteries: From Oxygen Reduction Electrochemistry to Cathode Catalysts. *Chem. Soc. Rev.* **2012**, *41*, 2172–2192. [[CrossRef](#)]
19. Wang, Z.-L.; Xu, D.; Xu, J.-J.; Zhang, X.-B. Oxygen Electrocatalysts in Metal–Air Batteries: From Aqueous to Nonaqueous Electrolytes. *Chem. Soc. Rev.* **2014**, *43*, 7746–7786. [[CrossRef](#)]
20. Zitolo, A.; Ranjbar-Sahraie, N.; Mineva, T.; Li, J.; Jia, Q.; Stamatina, S.; Harrington, G.F.; Lyth, S.M.; Krtil, P.; Mukerjee, S.; et al. Identification of Catalytic Sites in Cobalt-Nitrogen-Carbon Materials for the Oxygen Reduction Reaction. *Nat. Commun.* **2017**, *8*, 957. [[CrossRef](#)]
21. Ratso, S.; Kruusenberg, I.; Käärik, M.; Kook, M.; Saar, R.; Kanninen, P.; Kallio, T.; Leis, J.; Tammeveski, K. Transition Metal-Nitrogen Co-doped Carbide-Derived Carbon Catalysts for Oxygen Reduction Reaction in Alkaline Direct Methanol Fuel Cell. *Appl. Catal. B Environ.* **2017**, *219*, 276–286. [[CrossRef](#)]
22. Kaare, K.; Yu, E.; Käämbre, T.; Volperts, A.; Dobele, G.; Zhurish, A.; Niaura, G.; Tamasauskaitė-Tamasiunaite, L.; Norkus, E.; Kruusenberg, I. Biomass-Derived Graphene-like Catalyst Material for Oxygen Reduction Reaction. *ChemNanoMat* **2021**, *7*, 307–313. [[CrossRef](#)]
23. Sathiskumar, C.; Ramakrishnan, S.; Vinothkannan, M.; Kim, A.R.; Karthikeyan, S.; Yoo, D.J. Nitrogen-Doped Porous Carbon Derived from Biomass Used as Trifunctional Electrocatalyst toward Oxygen Reduction, Oxygen Evolution and Hydrogen Evolution Reactions. *Nanomaterials* **2020**, *10*, 76. [[CrossRef](#)] [[PubMed](#)]
24. Zang, W.; Kou, Z.; Pennycook, S.J.; Wang, J. Heterogeneous Single Atom Electrocatalysis, Where “Singles” Are “Married”. *Adv. Energy Mater.* **2020**, *10*, 1903181. [[CrossRef](#)]
25. Qiao, B.; Wang, A.; Yang, X.; Allard, L.F.; Jiang, Z.; Cui, Y.; Liu, J.; Li, J.; Zhang, T. Single-Atom Catalysis of CO Oxidation Using Pt₁/FeO_x. *Nat. Chem.* **2011**, *3*, 634–641. [[CrossRef](#)]
26. Choi, C.H.; Kim, M.; Kwon, H.C.; Cho, S.J.; Yun, S.; Kim, H.-T.; Mayrhofer, K.J.J.; Kim, H.; Choi, M. Tuning Selectivity of Electrochemical Reactions by Atomically Dispersed Platinum Catalyst. *Nat. Commun.* **2016**, *7*, 10922. [[CrossRef](#)]
27. Yin, P.; Yao, T.; Wu, Y.; Zheng, L.; Lin, Y.; Liu, W.; Ju, H.; Zhu, J.; Hong, X.; Deng, Z.; et al. Single Cobalt Atoms with Precise N-Coordination as Superior Oxygen Reduction Reaction Catalysts. *Angew. Chem. Int. Ed.* **2016**, *55*, 10800–10805. [[CrossRef](#)]
28. Borghei, M.; Lehtonen, J.; Liu, L.; Rojas, O.J. Advanced Biomass-Derived Electrocatalysts for the Oxygen Reduction Reaction. *Adv. Mater.* **2018**, *30*, 1703691. [[CrossRef](#)]
29. Mahbub, M.A.A.; Adios, C.G.; Xu, M.; Prakoso, B.; LeBeau, J.M.; Sumboja, A. Red Bean Pod Derived Heterostructure Carbon Decorated with Hollow Mixed Transition Metals as a Bifunctional Catalyst in Zn-Air Batteries. *Chem-Asian J.* **2021**, *16*, 2559–2567. [[CrossRef](#)]
30. Sumboja, A.; Prakoso, B.; Ma, Y.; Irwan, F.R.; Hutani, J.J.; Mulyadewi, A.; Mahbub, M.A.A.; Zong, Y.; Liu, Z. FeCo Nanoparticle-Loaded Nutshell-Derived Porous Carbon as Sustainable Catalyst in Al-Air Batteries. *Energy Mater. Adv.* **2021**, *2021*, 7386210. [[CrossRef](#)]
31. Wu, G.; Zelenay, P. Single-Atom Catalysts: A New Frontier in Heterogeneous Catalysis. *Acc. Chem. Res.* **2013**, *46*, 1878–1889. [[CrossRef](#)] [[PubMed](#)]
32. Zhao, D.; Shui, J.-L.; Chen, C.; Chen, X.; Repogle, B.M.; Wang, D.; Liu, D.-J. Iron imidazolate Framework as Precursor for Electrocatalysts in Polymer Electrolyte Membrane Fuel Cells. *Chem. Sci.* **2012**, *3*, 3200–3205. [[CrossRef](#)]
33. Jiao, L.; Zhang, R.; Wan, G.; Yang, W.; Wan, X.; Zhou, H.; Shui, J.; Yu, S.-H.; Jiang, H.-L. Nanocasting SiO₂ into Metal-Organic Frameworks Imparts Dual Protection to High-Loading Fe Single-Atom Electrocatalysts. *Nat. Commun.* **2020**, *11*, 2831. [[CrossRef](#)]
34. Martinez, U.; Babu, S.K.; Holby, E.F.; Chung, H.T.; Yin, X.; Zelenay, P. Progress in the Development of Fe-Based PGM-Free Electrocatalysts for the Oxygen Reduction Reaction. *Adv. Mater.* **2019**, *31*, 1806545. [[CrossRef](#)] [[PubMed](#)]
35. Wang, X.X.; Swihart, M.T.; Wu, G. Performance Enhancement and Degradation Mechanism Identification of a Single-Atom Co-N-C Catalyst for Proton Exchange Membrane Fuel Cells. *Nat. Catal.* **2019**, *2*, 578–589. [[CrossRef](#)]
36. Chen, G.; Liu, P.; Liao, Z.; Sun, F.; He, Y.; Zhong, H.; Zhang, T.; Zschech, E.; Chen, M.; Wu, G.; et al. Zinc-Mediated Template Synthesis of Fe-N-C Electrocatalysts with Densely Accessible Fe-N_x Active Sites for Efficient Oxygen Reduction. *Adv. Mater.* **2020**, *32*, 1907399. [[CrossRef](#)] [[PubMed](#)]

37. Hu, B.-C.; Wu, Z.-Y.; Chu, S.-Q.; Zhu, H.-W.; Liang, H.-W.; Zhang, J.; Yu, S.-H. SiO₂-Protected Shell Mediated Templating Synthesis of Fe–N-doped Carbon Nanofibers and Their Enhanced Oxygen Reduction Reaction Performance. *Energy Environ. Sci.* **2018**, *11*, 2208–2215. [[CrossRef](#)]
38. Fu, X.; Zamani, P.; Choi, J.-Y.; Hassan, F.M.; Jiang, G.; Higgins, D.C.; Zhang, Y.; Hoque, M.A.; Chen, Z. In Situ Polymer Graphenization Ingrained with Nanoporosity in a Nitrogenous Electrocatalyst Boosting the Performance of Polymer-Electrolyte-Membrane Fuel Cells. *Adv. Mater.* **2017**, *29*, 1604456. [[CrossRef](#)]
39. Zhu, C.; Shi, Q.; Xu, B.Z.; Fu, S.; Wan, G.; Yang, C.; Yao, S.; Song, J.; Zhou, H.; Du, D.; et al. Hierarchically Porous M–N–C (M = Co and Fe) Single-Atom Electrocatalysts with Robust MN_x Active Moieties Enable Enhanced ORR Performance. *Adv. Energy Mater.* **2018**, *8*, 1801956. [[CrossRef](#)]
40. Ye, Y.; Cai, F.; Li, H.; Wu, H.; Wang, G.; Li, Y.; Miao, S.; Xie, S.; Si, R.; Wang, J.; et al. Surface Functionalization of ZIF-8 with Ammonium Ferric Citrate toward High Exposure of Fe–N Active Sites for Efficient Oxygen and Carbon Dioxide Electroreduction. *Nano Energy* **2017**, *38*, 281–289. [[CrossRef](#)]
41. Jiang, R.; Li, L.; Sheng, T.; Hu, G.; Chen, Y.; Wang, L. Edge-Site Engineering of Atomically Dispersed Fe–N₄ by Selective C–N Bond Cleavage for Enhanced Oxygen Reduction Reaction Activities. *J. Am. Chem. Soc.* **2018**, *140*, 11594–11598. [[CrossRef](#)] [[PubMed](#)]
42. Guo, J.; Li, B.; Zhang, Q.; Liu, Q.; Wang, Z.; Zhao, Y.; Shui, J.; Xiang, Z. Highly Accessible Atomically Dispersed Fe–N_x Sites Electrocatalyst for Proton-Exchange Membrane Fuel Cell. *Adv. Sci.* **2021**, *8*, 2002249. [[CrossRef](#)]
43. Lee, S.H.; Kim, J.; Chung, D.Y.; Yoo, J.M.; Lee, H.S.; Kim, M.J.; Mun, B.S.; Kwon, S.G.; Sung, Y.-E.; Hyeon, T. Design Principle of Fe–N–C Electrocatalysts: How to Optimize Multimodal Porous Structures? *J. Am. Chem. Soc.* **2019**, *141*, 2035–2045. [[CrossRef](#)]
44. Wan, X.; Liu, X.; Li, Y.; Yu, R.; Zheng, L.; Yan, W.; Wang, H.; Xu, M.; Shui, J. Fe–N–C Electrocatalyst with Dense Active Sites and Efficient Mass Transport for High-Performance Proton Exchange Membrane Fuel Cells. *Nat. Catal.* **2019**, *2*, 259–268. [[CrossRef](#)]
45. Ghosh, S.; Basu, R.N. Multifunctional Nanostructured Electrocatalysts for Energy Conversion and Storage: Current Status and Perspectives. *Nanoscale* **2018**, *10*, 11241–11280. [[CrossRef](#)]
46. Wang, H.-F.; Chen, L.; Pang, H.; Kaskel, S.; Xu, Q. MOF-Derived Electrocatalysts for Oxygen Reduction, Oxygen Evolution and Hydrogen Evolution Reactions. *Chem. Soc. Rev.* **2020**, *49*, 1414–1448. [[CrossRef](#)]
47. Cai, X.; Lai, L.; Lin, J.; Shen, Z. Correction: Recent Advances in Air Electrodes for Zn–air Batteries: Electrocatalysis and Structural Design. *Mater. Horiz.* **2017**, *4*, 945–976. [[CrossRef](#)]
48. Chen, P.; Zhang, K.; Tang, D.; Liu, W.; Meng, F.; Huang, Q.; Liu, J. Recent Progress in Electrolytes for Zn–Air Batteries. *Front. Chem.* **2020**, *8*, 372. [[CrossRef](#)] [[PubMed](#)]
49. Fu, J.; Liang, R.; Liu, G.; Yu, A.; Bai, Z.; Yang, L.; Chen, Z. Recent Progress in Electrically Rechargeable Zinc–Air Batteries. *Adv. Mater.* **2019**, *31*, 1805230. [[CrossRef](#)]
50. Sa, Y.J.; Seo, D.-J.; Woo, J.; Lim, J.T.; Cheon, J.Y.; Yang, S.Y.; Lee, J.M.; Kang, D.; Shin, T.J.; Shin, H.S.; et al. A General Approach to Preferential Formation of Active Fe–N_x Sites in Fe–N/C Electrocatalysts for Efficient Oxygen Reduction Reaction. *J. Am. Chem. Soc.* **2016**, *138*, 15046–15056. [[CrossRef](#)]
51. Malonzo, C.D.; Shaker, S.M.; Ren, L.; Prinslow, S.D.; Platero-Prats, A.E.; Gallington, L.C.; Borycz, J.; Thompson, A.B.; Wang, T.C.; Farha, O.K.; et al. Thermal Stabilization of Metal–Organic Framework-Derived Single-Site Catalytic Clusters through Nanocasting. *J. Am. Chem. Soc.* **2016**, *138*, 2739–2748. [[CrossRef](#)] [[PubMed](#)]
52. Liang, H.-W.; Zhuang, X.; Brüller, S.; Feng, X.; Müllen, K. Hierarchically Porous Carbons with Optimized Nitrogen Doping as Highly Active Electrocatalysts for Oxygen Reduction. *Nat. Commun.* **2014**, *5*, 4973. [[CrossRef](#)] [[PubMed](#)]
53. Jaouen, F.; Lefèvre, M.; Dodelet, J.-P.; Cai, M. Heat-Treated Fe/N/C Catalysts for O₂ Electroreduction: Are Active Sites Hosted in Micropores? *J. Phys. Chem. B* **2006**, *110*, 5553–5558. [[CrossRef](#)] [[PubMed](#)]
54. Wang, X.; Li, Z.; Qu, Y.; Yuan, T.; Wang, W.; Wu, Y.; Li, Y. Review of Metal Catalysts for Oxygen Reduction Reaction: From Nanoscale Engineering to Atomic Design. *Chem* **2019**, *5*, 1486–1511. [[CrossRef](#)]
55. Zhang, H.; Hwang, S.; Wang, M.; Feng, Z.; Karakalos, S.; Luo, L.; Qiao, Z.; Xie, X.; Wang, C.; Su, D.; et al. Single Atomic Iron Catalysts for Oxygen Reduction in Acidic Media: Particle Size Control and Thermal Activation. *J. Am. Chem. Soc.* **2017**, *139*, 14143–14149. [[CrossRef](#)] [[PubMed](#)]
56. Lin, L.; Zhu, Q.; Xu, A.-W. Noble-Metal-Free Fe–N/C Catalyst for Highly Efficient Oxygen Reduction Reaction under Both Alkaline and Acidic Conditions. *J. Am. Chem. Soc.* **2014**, *136*, 11027–11033. [[CrossRef](#)] [[PubMed](#)]